Experimental and Numerical Study of the Propeller/Fixed Wing Interaction

Gilles Fratello,* Daniel Favier,† and Christian Maresca†
Université d'Aix-Marseille II, 13003 Marseille, France

With the advent of high-efficiency propellers as a propulsion alternative for the future, it has become necessary for the nature of the slipstream and its interference with aircraft components to be known over a wide range of operating conditions. A complementary experimental and computational investigation of the interaction between a propeller and a fixed wing is reported here. The experimental investigation is conducted on a propeller/nacelle wing configuration at low subsonic speeds. Tests performed on the propeller, nacelle, and wing provide the reciprocal influence of each element of the wind-tunnel configuration. The net slipstream influence on the wing aerodynamic behavior as well as the modification induced by the presence of the wing on the propeller thrust and torque coefficients are measured and discussed in this paper. The wing aerodynamic coefficients and the local chordwise distribution pressure distributions also have been measured at different spanwise sections. The computational approach is based on a lifting line method for blades modeling and a free wake analysis for the propeller slipstream associated with a panel method for the wing. The calculation code efficiency is checked by comparsions with pressure distributions measured on the wing.

Nomenclature

b = number of blades, $=4$
CD = drag coefficient of the wing, $=D/\frac{1}{2}\rho V_\infty^2 S$
CL = lift coefficient of the wing, $=L/\frac{1}{2}\rho V_\infty^2 S$
CM = moment coefficient of the wing, $=M/\frac{1}{2}\rho V_\infty^2 Sc$
Cp = pressure coefficient, $=(p-p_\infty)/\frac{1}{2}\rho V_\infty^2$
CT = traction coefficient of the propeller/nacelle/wing configuration, $=T/\frac{1}{2}\rho V_\infty^2 S$
c = wing chord section, $=1.2D=1.02$ m
D = propeller diameter, $=0.85$ m
Kp = total pressure coefficient through the rotating plane, $=(p_{t2}-p_{t1})/\rho n^2 D^2$
L = wing span, $=2D=1.70$ m
M = pitching moment of the wing around the quarter chord axis, N m
n = propeller rotating frequency, rps
$OXYZ$ = coordinates system defined in Fig. 2
P = propeller power, $=2\pi nQ$, W
p,p_t,p_∞ = static pressure, total pressure, and pressure at infinity, Pa
Q = propeller torque, N m
R = propeller radius, $=D/2$, m
r = radial coordinate from the axis of rotation, m
S = wing surface, $=Lc$, m^2
T = propeller thrust, N
t = time, s
U,V,W = velocity components defined in Fig. 1, m/s
V_∞,V_p = velocity at infinity, induced velocity due to the propeller slipstream, m/s
α = geometric incidence of the propeller/nacelle/wing configuration, deg
α_0 = mean pitch angle at $r/R=0.7$ of the propeller blade, deg
α_1 = wing geometric incidence at zero lift line, $=-2$ deg
γ = propeller operating parameter, $=V_\infty/nD$
η = propeller efficiency, $=\gamma\tau/\chi$
λ = propeller advance ratio, $=V_\infty/\omega R=\gamma/\pi$
ν = kinematic viscosity, m^2/s
ρ = air density, kg/m^3
τ = propeller thrust coefficient, $=T/\rho n^2 D^4$
χ = propeller power coefficient, $=P/\rho n^3 D^5$
ψ = blade azimuth angle, $=\Omega t$, deg
Ω = propeller rotational frequency, rad/s
ωt = phase of the period, deg

Subscripts
st,stat = steady conditions
inst = unsteady conditions
∞ = uniform flow conditions
i,ind = induced quantity

Superscripts
$\bar{}$ = time averaged quantity over a rotational period

Introduction

THE benefits expected in terms of fuel consumption and reduction of life-cycle costs have been a decisive factor in the renewed interest of propeller-type propulsion systems. The increasing cruise speed of current passenger flight has also stimulated efforts of aerodynamicists in the conception and design of advanced turboprop systems. As a counterpart, the use of such propellers as an aircraft propulsion system has accentuated the need of a better understanding, prediction, and treatment of the interference effects between the propeller and the other aircraft components, especially wings or fuselage. Aerodynamic performances, aircraft stability, and noise generation can be significantly affected by the interactions, and the installation design thus requires an adequate optimization in integrating the propulsion system. As an example, this design problem becomes particularly critical in such research programs as the Eurofar Tilt-Rotor project.[1]

In almost all experimental[2,3] and numerical[4–8] studies devoted to investigate the propeller/wing interaction problem, emphasis generally has been placed on the influence of the wake generated by the propeller either on the wing aero-

Presented as Paper 88-2531 at the AIAA 6th Applied Aerodynamics Conference, Williamsburg, VA, June 6–8, 1988; received June 14, 1989; revision received April 15, 1990; accepted for publication May 6, 1990.

*Graduate Student, Institut de Mécanique des Fluides.
†CNRS Senior Research Scientist, Institut de Mécanique des Fluides. Member AIAA.

dynamic behavior or on some part of the aircraft fuselage. However, the presence of the wing also has the effect to substantially change the wake geometry and the overall propeller performances. A proper investigation of the propeller/wing interaction problem thus requires to characterize both the propeller slipstream effect on the wing and the reciprocal influence of the wing presence on the propeller flowfield and performances.

The present work comprises a complementary experimental and computational effort that addresses the mutual influence problem between the propeller and the wing. In order to gain a physical understanding of the propeller/wing interaction phenomenon, it is first required that the entire flowfield generated in the isolated propeller case be perfectly known,[2] including both the rotary wing performances and the slipstream characteristics (wake geometry, tip vortex path, induced velocity field at different distances downstream of the rotating plane, etc.). An experimental modeling of the flowfield associated to the isolated propeller case has been obtained previously from the present group and has been reported in Refs. 9–11. Moreover, the corresponding numerical modeling has been formulated using a free wake analysis code called SMEHEL and is based on a lifting line method for the blade and a complete equilibrium procedure for the associated wake. A large check of the SMEHEL code efficiency to predict both overall and local aerodynamic quantities has been realized through extensive comparisons with test data obtained on an isolated propeller operating in a four-bladed configuration and over a wide range of parameters of the axial flight regime.[11,12]

In the present study, the experimental approach of the interaction problem is conducted on a model scale of a propeller/nacelle/wing configuration where the propeller is the same as in previous works.[9–12] The wind-tunnel configuration consists of a fixed rectangular wing joined by a nacelle to the propeller operating at subsonic speeds. From a series of forces and moments measurements successively performed on the wing, nacelle, propeller, and propeller/nacelle/wing ensemble, the specific airload contributions of each component of the propeller/nacelle/wing ensemble are obtained (e.g., thrust and power coefficients on the propeller, aerodynamic coefficients *CL*, *CD*, *CM* either on the wing or the nacelle). Chordwise pressure distributions on the wing surface have been measured additionally, either when the wing is isolated in the freestream of the wind tunnel or when the wing is immersed in the propeller slipstream. The wind-tunnel data tests are used to check the prediction efficiency of a numerical model formulated as a preliminary design tool for calculating the influence of the slipstream on the wing aerodynamic behavior. This calculation code, called COHV, consists of coupling the SMEHEL code previously developed[11,12] for the isolated propeller case with a singularities panel method for the fixed wing modeling.

Experimental Setup and Measurements Techniques

Tests were conducted at the Institut de Mécanique des Fluides de Marseille (IMFM) in the 3.3- × 2.2-m^2 S1-subsonic wind-tunnel open elliptical test section (length: 3 m). As sketched in Fig. 1, the complete setup includes the model propeller, nacelle, and fixed wing. The propeller (Marquis type: 0.85-m diam) is powered by an electrical motor. The motor and its torquemeter are housed in the nacelle. The four blades are cambered NACA 64A408 airfoil sections of variable thickness and chord. The tips are rectangular and the twist law is a nonlinear function of the blade radius as defined in Refs. 11 and 12. For the present tests, the fixed wing is supported by a mast equipped with a set of strain gauges for lift, drag, and moment measurements. The nacelle provides a smooth joint between the propeller and the wing. The nacelle wing is a small scale model of the nacelle wing installed on the Aérospatiale ATR-42 commuter airplane.

As described in Fig. 2a, the wing has a RA 18-43N1L1 airfoil section of 17% thickness. The angle α_1 between the zero lift line and the propeller axis is equal to -2 deg, as is the case on the actual ATR-42 airplane. The position of the wing with respect to the propeller also corresponds to the ATR-42 design ($h1 = 0.1c$) except that the distance d had to be reduced from $d = 0.84D$ to $d = 0.3D$, due to the available length of the open test section. The wing is built by stacking different elements, as illustrated in Fig. 2b. Behind the down-going blade side, the half wing is in one piece (right side in Fig. 2b). On the other side, behind the up-going blade, the wing is made of small movable pieces. One of them is equipped with 20 pressure transducers and another one with 20 skin friction gauges. Local chordwise pressure and skin friction distributions can thus be obtained at different positions of the wing span by moving the instrumented section of the wing. End plates also have been mounted at the tip of the fixed wing in order to provide a two-dimensional flow outside the influence of the propeller slipstream.

Inserted between the propeller and the wing, the nacelle represents 12% of the wing span. Between the wing and the nacelle, two thin pieces (3 mm thick) can be removed. In this case, as shown in Fig. 1, the wing is supported by a frame and is uncoupled to the nacelle so only the nacelle and propeller contributions are weighted. More details on the experimental setup capabilities and the associated measurements procedures can be found in Refs. 13 and 14.

It can be noticed that the net aerodynamic effect induced by the propeller slipstream on the wing cannot be obtained from a direct measurement. A series of measurements have to be realized in successive configurations of the three elements: propeller, nacelle, and wing (numbered from 1 to 6 in Fig. 3). Different algebraic operations are then performed to separate the contributions of each element (operations labeled a to h in Fig. 3). In Fig. 3, P refers to propeller, N to nacelle, W to wing, and WU to uncoupled wing configuration. For example, configuration 2 (PNWU) is an airload measurement performed on the propeller/nacelle/wing configuration. In this case, the wing is uncoupled, thus not weighted. Configuration 3 (NW) is a test without the propeller in which the nacelle and the wing are coupled.

For a given configuration in Fig. 3, the component of forces and moments to be measured is obtained as the sum of the different elements' contributions. For a given configuration and a given component, each contribution is referenced with a letter (*L* for lift, *T* for thrust, *D* for drag, *M* for pitching moment) added to the contributing element or group of elements, *i* indicates an induced effect. When the symbol (/) separates an element from a group of elements, it means the effect is induced by the first element to this group. For example, Li P/NW means lift induced by the propeller on the nacelle and wing. In some cases, as moment measurements in configuration 1 (PNW), as much as nine contributions are involved in the recorded test result. The purpose of the various combined operations is to extract the basic contributions of each element from the ensemble of data tests. How-

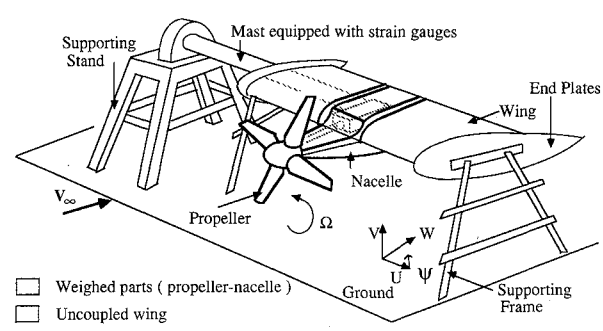

Fig. 1 Sketch of the propeller/nacelle/wing configuration—uncoupled wing mounting.

ever, it should be mentioned that it is not always possible to completely separate some specific contributions. As an example, in operation h, which is performed to obtain the induced effect of the propeller on the wing, the lift and drag contributions to the pitching moment cannot be obtained separately.

The present tests were conducted for two mean pitch angles α_0 of the propeller blade: $\alpha_0 = 27$ and 32.5 deg, while γ is varying from 0.7 to 1.0. The incidence angle of the propeller/nacelle/wing (Fig. 2a) was kept at the constant value $\alpha = 0$ deg. For the series of experiments presented here, only the mean values have been generally considered. They are obtained by averaging the recorded quantities over a period of the propeller rotation.

Experimental Results

The components *CL*, *CD*, and *CM* obtained for configuration 1 (PNW sketched in Fig. 4a) are presented in Figs. 4b–4d as a function of the advancing parameter γ. Concerning the lift coefficient (Fig. 4b), a slight increase from -0.04 to $+0.02$ may be observed when γ increases. The lift of the nacelle/wing without propeller (dashed line in Fig. 4a) is recovered around $\gamma = 0.89$ and for $\alpha_0 = 27$ deg. An increase of up to $\alpha_0 = 32.5$ deg (corresponding to an increase of the propeller thrust[11,12]) reduces the lift coefficient but does not modify the evolution shape of *CL* as a function of γ. This trend is also shown on the *CM* component (Fig. 4d), where the nose-up effect is amplified for $\alpha_0 = 32.5$ deg. For a specific value of α_0, since the propeller thrust is reduced with increasing values of γ, the moment tends to become nose down as γ increases as in the case of uniform flow (dashed line in Fig. 4d).

In fact, the main influence of the propeller slipstream appears to concern the thrust component as shown in Fig. 4c. The thrust coefficient decreases as γ increases (i.e., for a given α_0, as the propeller thrust reduces) and it increases with α_0 (i.e., for a given γ, the propeller thrust increases). At $\gamma = 1$ and $\alpha_0 = 27$ deg, the thrust of the propeller can just balance the drag of the nacelle/wing.

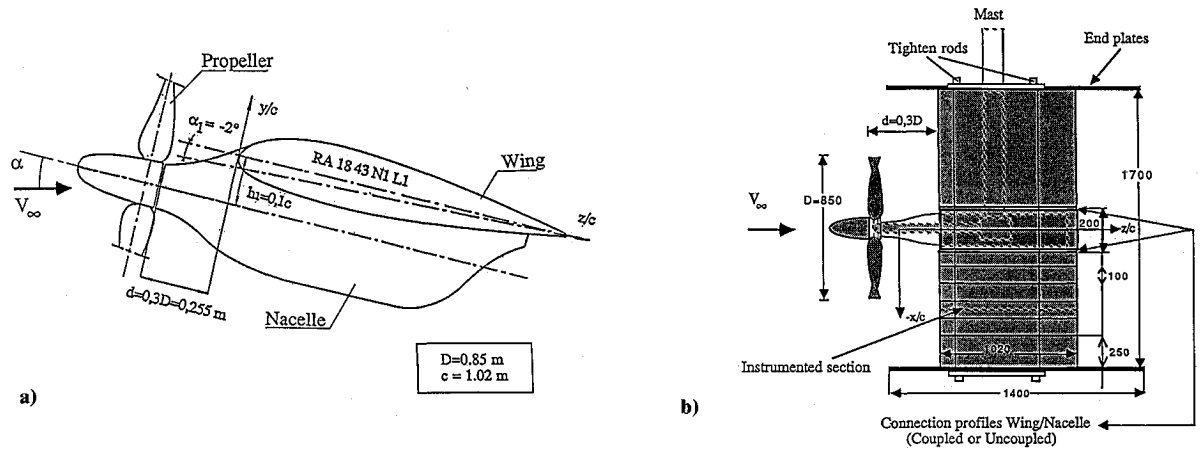

Fig. 2 Wind-tunnel test rig: a) side view; b) top view.

N° Config. / Torsor Component	1 [P-N-W]	2 [P-N-WU]	3 [N-W]	4 [N-WU]	5 [P-N]	6 [N]
LIFT	LW + Li P/W + LNW + Li P/NW	LNW+ Li P/NW	LW + LNW	LNW	LN + Li P/N	LN
THRUST-DRAG	DW + TPW + Di P/W + DNW + Di P/NW	TPW + DNW + Di P/NW	DW + DNW	DNW	TP + DN + Di P/N	DN
PITCHING MOMENT	MLW + MDW + MTPW + MLi P/W + MDi P/W + MLNW + MDNW + MLi P/NW + MDi P/NW	MTPW + MLNW + MDNW + MLi P/NW + MDi P/NW	MLW + MDW + MLNW + MDNW	MLNW + MDNW	MTP + MLN + MDN + MLi P/N + MDi P/N	MLN + MDN

Opération / Torsor Component	a (5) - (6)	b (3) - (4)	c (2) - (4)	d (1) - (2)	e (2) - (5)	f (4)	g (6)	h {(1)-(2)} - {(3)-(4)}
LIFT	Li P/N	LW	Li P/NW	LW + Li P/W	LNW - LN + Li P/W - Li P/N	LNW	LN	Li P/W
THRUST-DRAG	TP + Di P/N	DW	TPW + Di P/NW	DW + Di P/W	TPW - TP + DNW - DN + Di P/NW - Di P/N	DNW	DN	Di P/W
PITCHING MOMENT	MTP + MLi P/N + MDi P/N	MLW + MDW	MTPW + MLi P/NW + MDi P/NW	MLW + MDW + MLi P/W + MDi P/W	MTPW - MTP + MLi P/NW - MLi P/N + MDi P/NW - MDi P/N + MLNW - MLN + MDNW - MDN	MLNW + MDNW	MLN + MDN	MLi P/W + MDi P/W

Fig. 3 Test configurations and algebraic operations on the aerodynamic components.

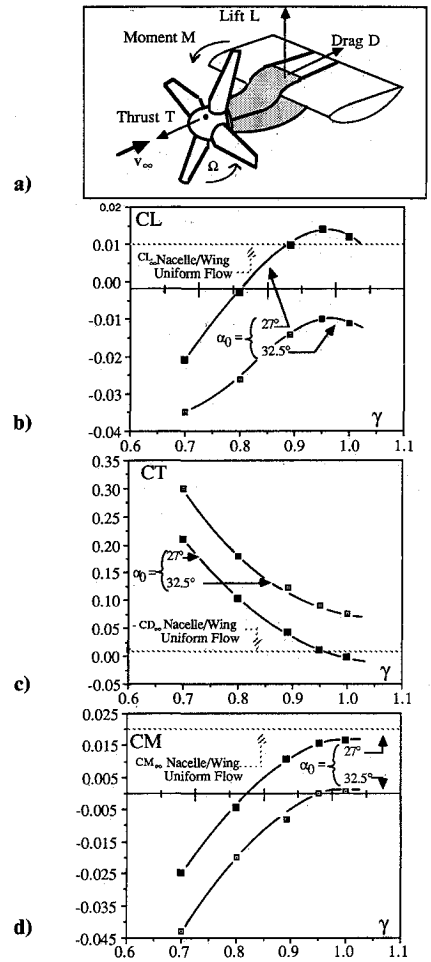

Fig. 4 *CL, CT, CM* **coefficients as a function of** γ **at** $\alpha = 0$ **deg in the P/N/W configuration.**

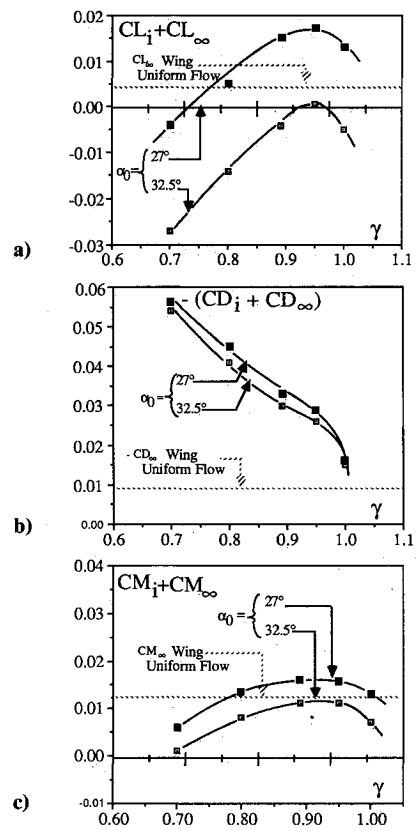

Fig. 5 $(CL_i + CL_\infty)$, $(CD_i + CD_\infty)$, $(CM_i + CM_\infty)$ **as a function of** γ **at** $\alpha = 0$ **deg: effect of the uniform flow and the slipstream on the wing.**

Operation d in Fig. 3 [configuration 1 (PNW) – configuration 2 (PNWU)] provides the three airloads and moment components of the wing ($CL_\infty + CL_i$, $CD_\infty + CD_i$, $CM_\infty + CM_i$) induced by V_∞ and the propeller slipstream. These coefficients are presented as a function of γ in Figs 5a–5c. Also in Fig. 5, plotted in a dashed line, are the uniform flow values without the nacelle obtained via operation b (see Fig. 3). The combined influences of the upstream velocity V_∞ and the propeller slipstream mainly concern the drag coefficient of the wing, especially at low values of γ (Fig. 5b) where the drag is significantly increased. When the propeller thrust is small ($\gamma \approx 1$), the drag recovers the value obtained in the uniform flow. The pitch angle α_0 has little effect on the drag coefficient compared to the lift and moment coefficient (Figs. 5a and 5c). At low values of γ, $CL_\infty + CL_i$ is below the lift coefficient CL_∞ of the wing alone. This net loss of lift due to the slipstream is recovered around $\gamma = 0.8$ for $\alpha_0 = 27$ deg; for $\alpha = 32.5$ deg, the lift coefficient remains below the uniform flow value. In Fig. 5c, the moment coefficient $CM_\infty + CM_i$ is nose down for the range of γ investigated and is close to the uniform flow value.

The net influence of the slipstream is clearly illustrated in Fig. 6 where operation h [(conf.1 – conf.2) – (conf.3 – conf.4)] gives the load effect of the slipstream alone on the fixed wing. When compared to Fig. 5, it can be observed that the slipstream effects are predominant regarding the *CL* and *CD* levels since they are very similar in Figs. 5a, 5b, 6a, and 6b. On the other hand, the uniform flow has a major effect on the moment coefficient *CM* since it remains around zero (Fig. 6c) for the range of γ considered.

The net slipstream influence on the wing can finally be characterized by the following points: 1) an increase of the drag coefficient CD_i compared to CD_∞ as the thrust of the propeller increases ($CD_i/CD_\infty = 4.7$ at $\gamma = 0.7$), 2) a decrease of CL_i compared to CL_∞ when the thrust of the propeller is high, and 3) a slight nose-up influence on the moment coefficient around $\gamma = 0.7$.

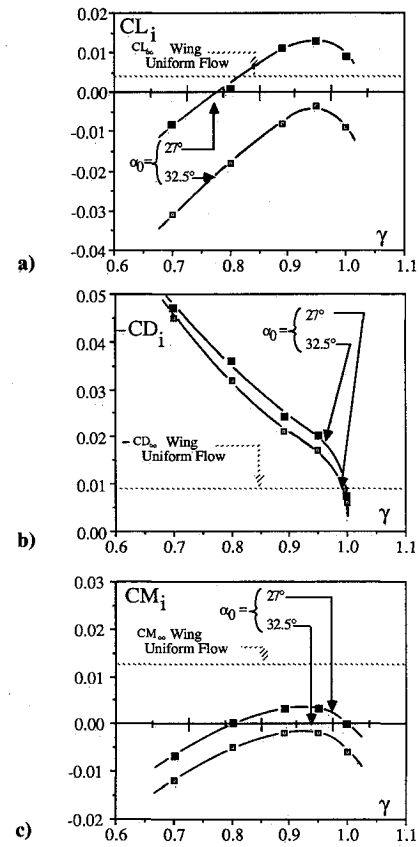

Fig. 6 (CL_i, CD_i, CM_i) **induced coefficients as a function of** γ **at** $\alpha = 0$ **deg: net influence of the slipstream on the wing.**

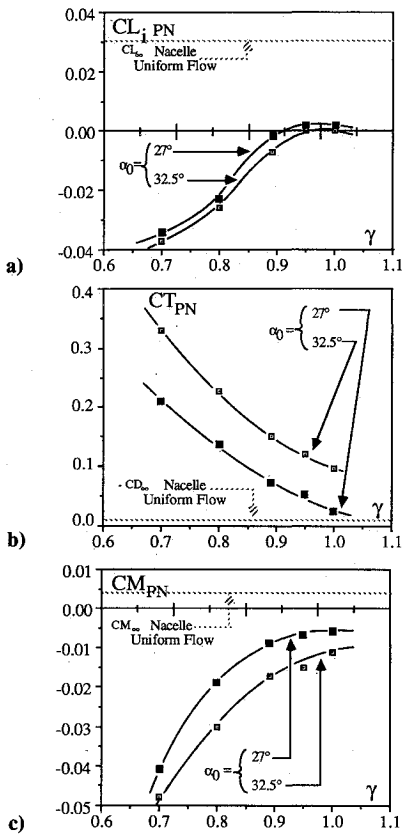

Fig. 7 (CL_i/N, CD_i/N, CM_i/N) as a function of γ at $\alpha = 0$ deg: effect of the slipstream on the nacelle.

When considering the effect of the slipstream on the nacelle alone, operation a (see Fig. 3) indicates that only the lift reveals a pure slipstream effect. The drag cannot be measured without the thrust of the propeller since the nacelle cannot be uncoupled from the propeller. Therefore, the moment coefficient still contains the propeller contribution. As already observed on the wing, the lift coefficient decreases with γ, but $CL_{P/N}$ remains well below $CL_{\infty N}$ (Fig. 7a). In Fig. 7b, the C_T evolution is mainly produced by the thrust of the propeller. The moment coefficient (Fig. 7c) is below the moment coefficient of the nacelle alone but closer to zero than it was with the wing in Fig. 5d. The moment tends to become nose down as γ increases. In uniform flow, the nacelle alone is slightly nose down ($CM_{\infty N} > 0$).

Concerning the local influence of the slipstream on the wing, the chordwise pressure distributions have been measured at the three stations of the up-going blade side [$X/(L/2) = -0.647, -0.412, -0.1765$] and then integrated. The corresponding mean span loading is compared in Fig. 8 ($\gamma = 0.89$, $\alpha_0 = 32.5$ deg, $\alpha_1 = -2$ deg, $\alpha = 0$ deg) to the overall values directly measured with the strain gauge technique. These overall measurements are obtained in the case of the wing placed in uniform flow alone from operation b [NW-NWU] and in the case of the wing submitted to both the uniform flow and the slipstream from operation d [PNW-PNWU].

With the slipstream, the integration of Cp distributions shows (Fig. 8a) an increase of the span lift coefficient behind the up-going blade at a level exceeding the values deduced by the strain gauge measurements either in the uniform flow alone V_∞ (dotted line) or in the flow resulting of V_∞ plus the slipstream influence (dashed line). On the other hand, the integration of the uniform flow Cp distributions (without slipstream influence) gives a reduction of $\overline{CL}$ toward the middle span of the wing at a level well below the strain gauge measurements. Outside the slipstream, the lift coefficient tends to recover the strain gauge measurement level. From the

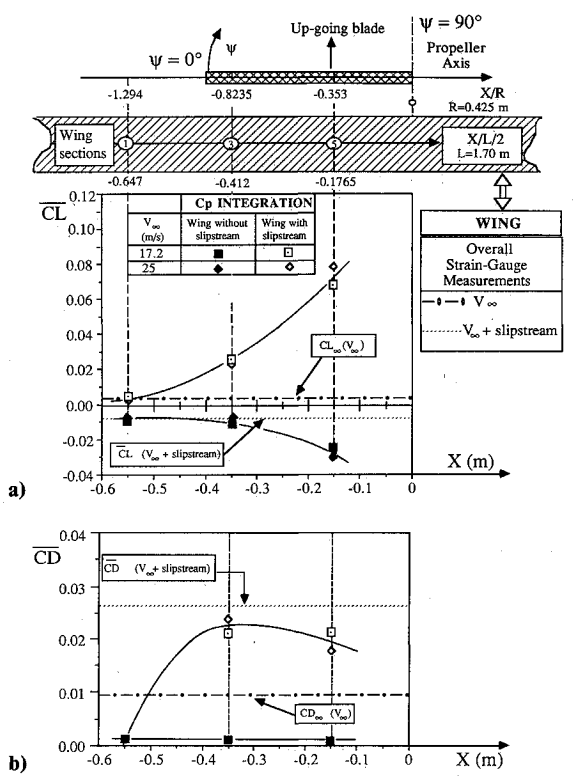

Fig. 8 Spanwise distribution of $\overline{CL}$ and $\overline{CD}$ as deduced from Cp integration and strain gauge measurements: $\alpha = 0$ deg; $\gamma = 0.89$; $\alpha_0 = 32.5$ deg.

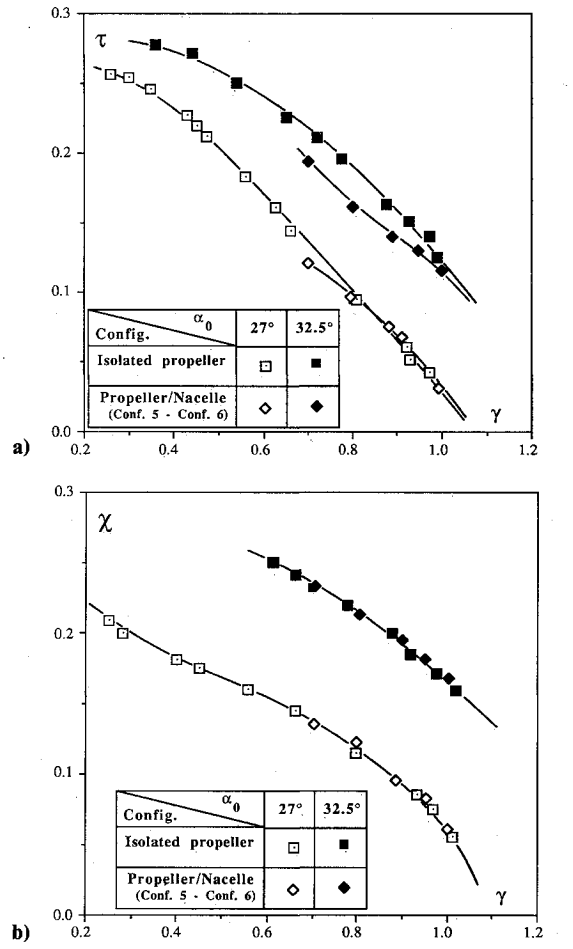

Fig. 9 Influence of the presence of the nacelle on the propeller performances: a) $\tau = \tau(\gamma)$; b) $\chi = \chi(\gamma)$.

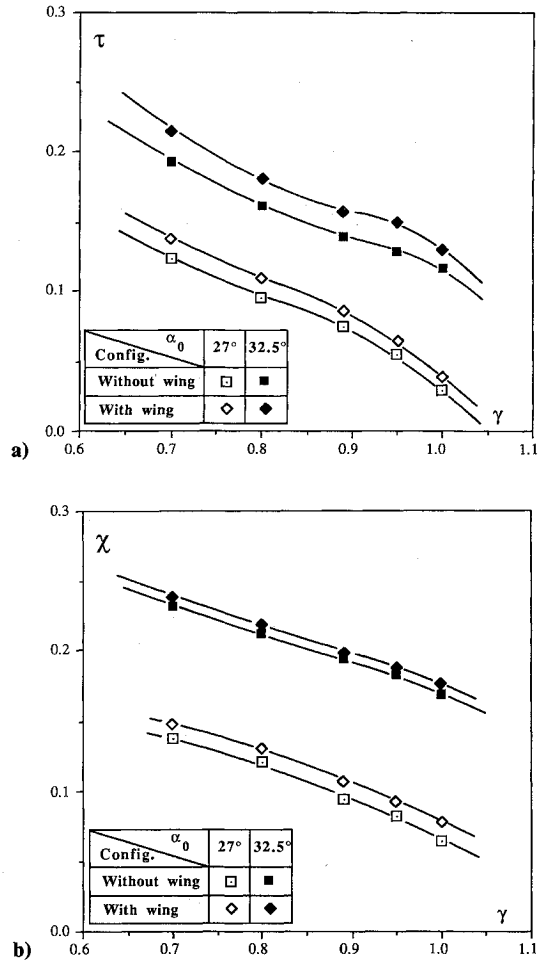

Fig. 10 Influence of the presence of the wing on the propeller performances: a) $\tau = \tau(\gamma)$; b) $\chi = \chi(\gamma)$.

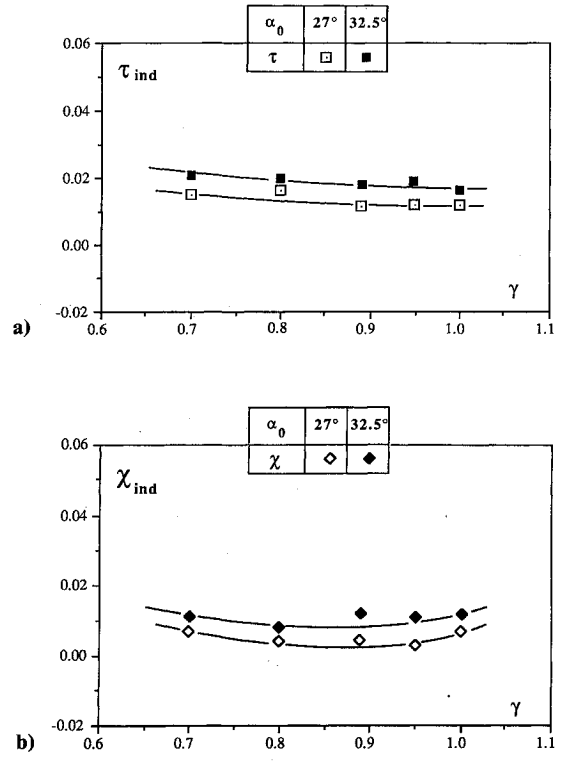

Fig. 11 Induced coefficients τ_{ind}, χ_{ind} as a function of γ at $\alpha = 0$ deg: net influence of the wing on the propeller performances.

results in Fig. 8b, it can be concluded that the drag coefficients estimated from the *Cp* distributions are underestimated compared to the strain gauge measurements in both cases.

From all of the above results, the propeller slipstream is shown to induce significant changes on the nacelle and wing load coefficients. However, interaction effects also imply a modification of the slipstream axisymmetry due to the presence of the nacelle/wing that, in turn, induces local modifications in the propeller rotation plane and changes in the propeller performances.

Operation a (Fig. 3) gives the thrust of the propeller in the presence of the nacelle. Since the nacelle is always coupled, the drag induced by a slipstream on the nacelle also contributes to the thrust measurement. In Fig. 9a, the thrust coefficient, thus obtained from operation a, is presented vs the operating parameter γ and for two values of the blade pitch angle ($\alpha_0 = 27$ and 32.5 deg). The thrust coefficient of the isolated propeller (obtained in a previous series of experiments without nacelle[9]) is also plotted in this figure. The reduction of thrust due to the nacelle is particularly significant for the higher loading values of the propeller at $\alpha_0 = 32.5$ deg. A slight change of slope ($\partial\tau/\partial\gamma$) can also be noted. However, the above observations are not found on the power coefficient plots in Fig. 9b, where the induced effect of the nacelle on the propeller torque appears to be significantly reduced.

The propeller performance coefficients obtained with and without the wing, are shown in Figs. 10a and 10b and reveal the reciprocal influence of the wing on the propeller. This influence, as expected, is more significant than the nacelle one, especially on the power coefficient probably caused by the straightening effect of the wing on the propeller slipstream. For both values of α_0 considered, the wing induces an increase of the τ and χ coefficients.

From the previous results, the respective thrust and power induced coefficients τ_{ind} and χ_{ind} can be obtained. They are presented in Figs. 11a and 11b as a function of γ. The presence of the wing appears to have an influence almost

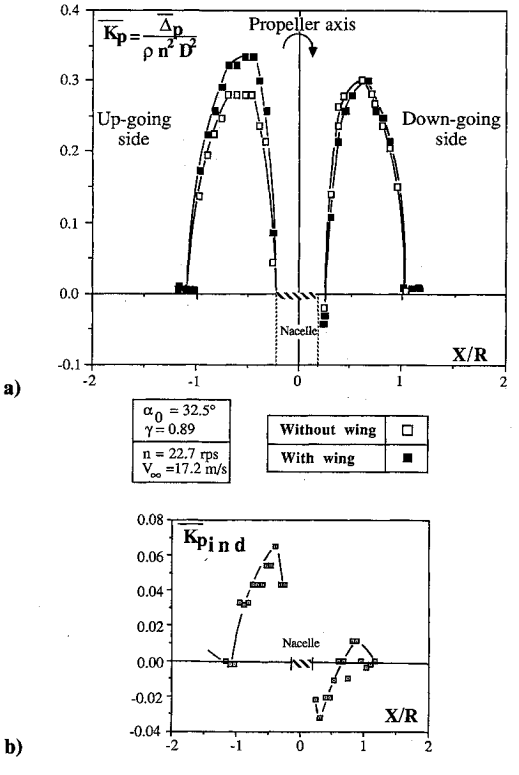

Fig. 12 Spanwise distribution of total pressure coefficients: a) $\overline{Kp} = \overline{Kp}(X/R)$ with and without wing; b) $\overline{Kp}_{ind}$ coefficient induced by the wing.

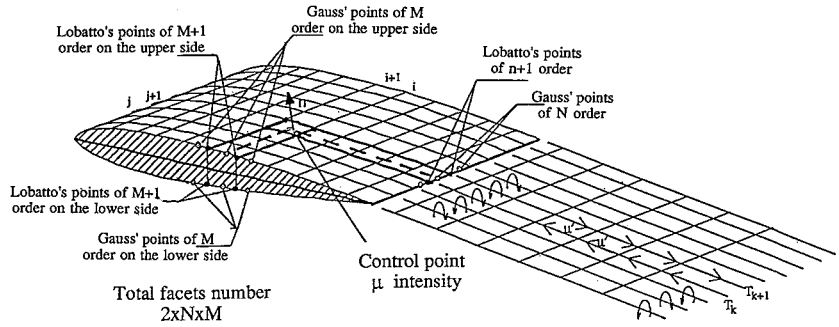

Fig. 13 Panel wing modeling and shed vorticity.

constant on the thrust and power coefficient ($\tau_{ind} \approx 0.02$ and $\chi_{ind} \approx 0.01$). In the range of γ considered ($0.7 \leq \gamma \leq 1$), the induced effect of the wing on the propeller is given by the rate of increase of the thrust and power coefficients as

$$\tau_{ind}/\tau_{without\ wing} = (\tau_{with\ wing} - \tau_{without\ wing})/\tau_{without\ wing} = 14\%$$

$$\chi_{ind}/\chi_{without\ wing} = (\chi_{with\ wing} - \chi_{without\ wing})/\chi_{without\ wing} = 8\%$$

It should be noted that the propeller had to operate at a constant rotating frequency n; thus, this increase of thrust and power coefficients results in an increase of power from the electric motor.

When considering the overall propeller performances with and without the wing, it appears that the total pressure jump Δp through the rotating plane might provide valuable information, both on the wake geometry distortion and on the modification of the blade loading repartition. The pressure difference Δp has been deduced from measurements performed just upstream and downstream of the rotating disk along a line parallel to the wing span at $y = 0$ and $\alpha_0 = 32.5$ deg; $\gamma = 0.89$. The mean total pressure coefficient $\overline{Kp} = \overline{\Delta p}/\rho n^2 D^4$, obtained by time averaging over the period the pressure jump Δp, is plotted in Fig. 12a as a function of the wing spanwise direction X/R. Also shown in this figure is the same quantity measured in same conditions but without the wing.

The comparison of the two pressure jump curves in Fig. 12a exhibits that, behind the up-going blade, the presence of the wing induces a significant increase of $\overline{Kp}$ and a displacement of the maximum value toward the propeller axis. Behind the down-going blade, the maximum $\overline{Kp}$ value is unchanged, but the curve is moved slightly toward the outboard of the propeller disk. Outside the disk and near the nacelle, $\overline{Kp}$ tends to zero.

From these results, the induced coefficient $\overline{Kp}_{ind}$ due to the wing presence is deduced from the measurements realized with and without the wing and is plotted in Fig. 12b. The net gain behind the up-going blade extends all along the blade radius, whereas behind the down-going blade, a loss of $\overline{Kp}$ up to $X/R = 0.6$ and a positive induced $\overline{Kp}$ up to $X/R = 1.0$ are obtained. On both sides, the maximum values are reached near the nacelle for $|X/R| < 0.4$.

Numerical Results

As mentioned previously, the numerical modeling of the interaction effects between the propeller and the wing is undertaken here using the COHV code developed at IMFM by coupling[13,14] a singularities panel method distributed on the wing and the SMEHEL free wake analysis code previously validated in the isolated propeller case.[11,12] However, due to the difficulty to take into account the complex flowfield environment inherent to the mutual interferences, it has been decided, in this first version of the COHV code, to neglect the influence of the wing on the propeller since the main interest was on the wing. Thus, the actual numerical analysis is limited to the modeling of the slipstream influence on the wing aerodynamic behavior, and the reciprocal modeling of the wing influence on the propeller performance will be

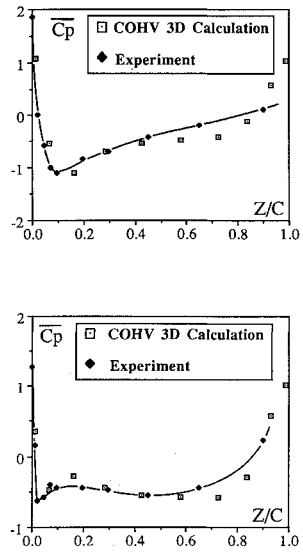

Fig. 14 Comparison calculation/experiment on the mean pressure coefficient $\overline{Cp}$ as a function of Z/c at $X/L = -0.22$: a) upper side; b) lower side.

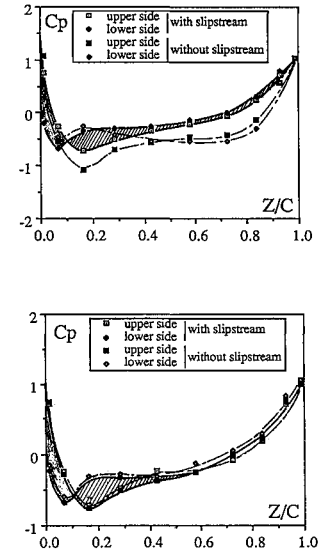

Fig. 15 Cp distributions calculated without and with slipstream influence ($\psi = 0$ deg) at $\alpha = 0$ deg: a) $X/L = -0.22$; b) $X/L = -0.51$.

undertaken in a future development of the COHV calculation code.

Within this frame, the present calculation model considers the wing immersed in the slipstream of the propeller that induces in all of the space an increase of the velocity and swirl, resulting in a modification of the flowfield surrounding the wing. The potential φ is then the sum of the different contributions of the uniform and wake flows ($\varphi_\infty + \varphi_s$) and of the wing potential of perturbation φ_w as

$$\varphi(x,y,z,t) = \varphi_\infty + \varphi_s(x,y,z,t) + \varphi_w(x,y,z,t)$$

The associated velocity field is then

$$V(x,y,z,t) = V_\infty + V_s(x,y,z,t) + \text{grad}[\varphi_w(x,y,z,t)]$$

and the total potential φ is obtained by solving the Laplace equation:

$$\Delta\varphi(x,y,z,t) = 0$$

In order to account for the velocity field induced by the isolated propeller and its associated wake, the SMEHEL code provides a complete wake equilibrium procedure decribed in Refs. 11 and 12. In this procedure, the propeller blade is represented by a lifting line and the basic equations are solved in a rotating frame attached to the blade. From the ends of each blade vortex element (N_p elements on the blade), N_{p+1} trailing vortex filaments leave the blade to form the wake. Moreover, each vortex filament that forms the near free wake region is continued in the far wake and contributes to form a semi-infinite cylinder of constant vorticity ($d\Gamma/dr$). That means that no distortions of the wake geometry and tip vortex paths have been introduced in the present version of the calculation code.

Concerning the wing, it has been represented by singularities distributed on a 20×20 mesh on each side as sketched in Fig. 13. The mesh generation is based on Lobatto's points on a segment $[-1, +1]$, whereas the panel control points are Gauss points. The vortex sheet issued from the wing is considered as a plane surface with a similar mesh and singularity distribution to the wing. The coupling between the propeller slipstream and the wing is obtained by imposing a Neuman's condition on the wing surface.

The evaluation of the prediction efficiency of the previously described calculation method has first concerned the mean chordwise pressure distributions $\overline{Cp}$ along the wing span. An example of comparison calculation/experiment is presented in Fig. 14, where the upper side and lower side $\overline{Cp}$ distributions are plotted as a function of the chordwise coordinate Z/c in the case of a propeller operating parameter $\gamma = 0.89$, $V_\infty = 17.2$ m/s, and for the wing span section $X/L = -0.22$ located behind the up-going propeller blade. Except near the trailing-edge region, the measured $\overline{Cp}$ distributions are shown to be well predicted by the calculation model. It can be noticed that the discrepancy exhibited near the trailing edge is also present when the wing is placed alone in the uniform flow, and, thus, this discrepancy has to be attributed to the mesh size definition in this region of the wing sections.

In Figs. 15a and 15b, the Cp distributions calculated by the COHV code with and without the slipstream are presented for two span locations behind the up-going blade: $X/L = -0.22$ and $X/L = -0.51$. When the slipstream is present, the instantaneous Cp distributions are plotted at the azimuth $\psi = 0$ deg of the blade rotation (i.e., when the blade is passing just in front of the leading edge of the wing).

At $X/L = -0.22$, the results indicate that the slipstream has the ability to, on the one hand, reduce the negative lift area obtained in the uniform flow case in the region $0 \leq Z/c \leq 0.12$ (dark region noted S1 in Fig. 15a) and, on the other hand, increase the positive lift area of the uniform flow case in the region $0.12 \leq Z/c \leq 0.40$ (hachured region noted S2 in Fig. 15a). Consequently, the local lift coefficient calculated from the Cp distributions of Fig. 15a with the slipstream would show an increase in lift equivalent to the one observed in Fig. 8 by integrating the Cp distributions at the same spanwise position. These results confirm the good efficiency of the calculation model in predicting characteristic features of the interaction process that have been also exhibited by experiments.

In the same way, at the spanwise position $X/L = -0.51$ (Fig. 15b), which is located near the slipstream limit, the results show that both calculations with and without the slipstream are very close. The regions noted S1 and S2 are shown to remain similar when the slipstream is added on the wing. Thus, the increase of local lift due to the slipstream remains small, in this case, and is well correlated by the experimental results previously discussed in Fig. 8.

Conclusions

In the present work, an experimental investigation has been conducted on different element combinations of a propeller/nacelle/wing configuration to study both the propeller slipstream influence on the aerodynamic mean loads of the nacelle/wing and the reciprocal influence of the wing on the propeller performances. For the range of parameters considered ($0.7 < \gamma < 1$, $\alpha = 0$ deg) the main slipstream effects on the wing are the following.

1) A significant increase of the mean drag of the wing compared to the uniform flow drag. A ratio of CD_i/CD_∞ up to 5 has been measured at the maximum thrust value of the propeller.

2) A decrease of the mean induced lift coefficient compared to CL_∞ at low values of γ.

3) The moment coefficient remains almost unchanged.

The reciprocal nacelle/wing influence on the propeller performance has revealed an increase of the thrust and power coefficients. For the range of investigated parameters (α_0,γ), the mean induced effect has been obtained as

$$\tau_{\text{ind}}/\tau_{\text{without wing}} = 14\%; \qquad \chi_{\text{ind}}/\chi_{\text{without wing}} = 8\%$$

Moreover, the measurements of the pressure jump coefficients $\overline{Kp}$ through the rotating plane show that the wing presence induces a significant modification of the radial loading distribution on the propeller blade. This modification in the loads and circulation distributions should be taken into account in any attempt at calculating the mutual interference effects.

The experimental results have been used to check the prediction efficiency of the COHV calculation model formulated in a simplified version. This formulation consists of considering the wing as immersed in the propeller slipstream and neglecting the reciprocal influence of the wing on the slipstream. Nevertheless, the present results have shown that the calculated mean pressure distributions $\overline{Cp}$ were in good agreement with the corresponding experimental distributions measured on the wing. The actual version of the COHV code already gives a correct estimation of the instantaneous interaction effects as a function of the blade azimuth angle. Obviously, this calculation code version must be improved to get a reliable tool for predicting all of the mutual interference effects. An attempt will be made in future work by accounting for the reciprocal influence of the wing on the propeller slipstream distortion using an iterative procedure.

The future experimental studies will also provide the instantaneous behaviors of the loads and moments coefficients and pressure distributions as a function of the blade rotation. These measurements will be compared to the instantaneous calculated values deduced from the new developments of the COHV code.

Acknowledgments

The present research has been supported by the Direction des Recherches Etudes et Techniques under Grant 85/115. The authors would like to thank their colleague Frédéric Pous for his help in preparing the drawings of this paper.

References

[1]Andres, J., Hubert, H., and Renaud, J., "The Tilt-Rotor Aircraft: A Response to the Future. From European Interrogations to EUROFAR Actions," *Proceedings of the 12th European Rotorcraft Forum*, Garmisch-Partenkirchen, Sept. 1986.

[2]Aljabri, A. S., and Hughes, A. C., "Wind Tunnel Investigation of the Interaction of Propeller Slipstream with Nacelle/Wing/Flap Combinations," AGARD CP 366, Paper 21, Oct. 1984.

[3]Howard, R. M., Miley, S. J., and Bruce, J. H., "Investigation of the Effects of the Propeller Slipstream on the Laminar Wing Boundary Layer," General Aviation Aircraft Meeting and Exposition, Wichita, KS, Paper 850859, April 1985.

[4]Rizk, M. H., "Propeller Slipstream/Wing Interaction in the Transonic Regime," *Journal of Aircraft*, Vol. 18, No. 3, 1981, pp. 184–191.

[5]Kirmann, C., Rousseau, A., and Yermia, M., "Calcul du Souffle Moyen d'une Hélice et de son Influence sur les Performances d'un Avion," *L'Aéronautique et l'Astronautique*, No. 104, 1984, pp. 1–45.

[6]Johnson, W., "Recent Developments in Rotary Wing Aerodynamic Theory," *AIAA Journal*, Vol. 24, No. 8, 1986, pp. 1219–1244.

[7]Bousquet, J. M., "Méthodes Aérodynamiques Utilisées en France pour l'Etude des Hélices pour Avions Rapides," AGARD CP 366, Paper 2, Oct. 1984.

[8]Ting, L., Liu, C. H., and Kleinstein, G., "Interference of Wing and Multipropellers," *AIAA Journal*, Vol. 10, No. 7, 1972, pp. 906–914.

[9]Favier, D., and Maresca, C., "Etude du Sillage d'une Hélice Aérienne," AGARD CP 366, Paper 15, Oct. 1984.

[10]Favier, D., Nsi Mba, M., Barbi, C., and Maresca, C., "A Free Wake Analysis for Hovering Rotors and Advancing Propellers," *Vertica*, Vol. 11, No. 3, 1987, pp. 493–511.

[11]Favier, D., Maresca, C., Nsi Mba, M., and Barbi, C., "Experimental and Numerical Aerodynamic Study of Rotors and Propellers Operating in Several Flight Conditions," *Proceedings of the 2nd International Conference on Basic Rotorcraft Research*, Univ. of Maryland, College Park, MD, Feb. 1988.

[12]Favier, D., Ettaouil, A., and Maresca, C., "Numerical and Experimental Investigation of Isolated Propeller Wakes in Axial Flight," *Journal of Aircraft*, Vol. 26, No. 9, 1989, pp. 837–846.

[13]Ettaouil, A., "Etude Numérique du Champ Aérodynamique d'une Hélice Aérienne Isolée ou en Interaction avec une Voilure-Validation par Comparaison avec l'Expérience," Ph.D. Dissertation, Université Aix-Marseille II, Marseille, France, No. 207.208.87.24, Sept. 1987.

[14]Favier, D., Maresca, C., and Nsi Mba, M., "Etude de l'Interaction Souffle d'Hélice/Voilure et Etude du Champ Aérodynamique d'un Rotor d'Hélicoptère en Vol Stationnaire et d'Avancement," Rapport de fin de contrat, Convention D.R.E.T. No. 85/115, Dec. 1987.